Gravitational Wave Signatures of Hyperaccreting Collapsar Disks

Kei Kotake[1,2], Tomoya Takiwaki[2], and Seiji Harikae[3]

[1]*Division of Theoretical Astronomy, National Astronomical Observatory of Japan, 2-21-1, Osawa, Mitaka, Tokyo, 181-8588, Japan*

`kkotake@th.nao.ac.jp`

[2]*Center for Computational Astrophysics, National Astronomical Observatory of Japan, 2-21-1, Osawa, Mitaka, Tokyo, 181-8588, Japan*

[3]*Quants Research Department, Financial Engineering Division, Mitsubishi UFJ Morgan Stanley Securities Co., Ltd., Marunouchi Bldg., 2-4-1, Marunouchi, Chiyoda-ku, Tokyo, 100-6317*

ABSTRACT

By performing two-dimensional special relativistic (SR) magnetohydrodynamic simulations, we study possible signatures of gravitational waves (GWs) in the context of the collapsar model for long-duration gamma-ray bursts. In our SR simulations, the central black hole is treated as an absorbing boundary. By doing so, we focus on the GWs generated by asphericities in neutrino emission and matter motions in the vicinity of the hyperaccreting disks. We compute nine models by adding initial angular momenta and magnetic fields parametrically to a precollapse core of a $35 M_\odot$ progenitor star. As for the microphysics, a realistic equation of state is employed and the neutrino cooling is taken into account via a multiflavor neutrino leakage scheme. To accurately estimate GWs produced by anisotropic neutrino emission, we perform a ray-tracing analysis in general relativity by a post-processing procedure. By employing a stress formula that includes contributions both from magnetic fields and special relativistic corrections, we study also the effects of magnetic fields on the gravitational waveforms. We find that the GW amplitudes from anisotropic neutrino emission show a monotonic increase with time, whose amplitudes are much larger than those from matter motions of the accreting material. We show that the increasing trend of the neutrino GWs stems from the excess of neutrino emission in the direction near parallel to the spin axis illuminated from the hyperaccreting disks. We point out that a recently proposed future space-based interferometer like Fabry-Perot type DECIGO would permit the detection of these GW signals within ≈ 100 Mpc.

Subject headings: massive stars: collapse — gamma-ray bursts — gravitational waves — neutrinos — hydrodynamics

1. Introduction

Gamma-ray bursts (GRBs) are one of the most energetic phenomena in the universe. Thanks to *Swift* observations[1], it has now become evident that GRBs are basically categorized into two, namely short-hard and long-soft bursts (e.g., Hjorth & Bloom (2011); Nakar (2007) for recent reviews). More surprisingly, GRBs with some mixed features of the two types have been reported (e.g., Gehrels et al. (2006), Gal-Yam et al. (2006)) possibly necessitating a new classification (Lü et al. 2010). The mystery of their central engines seems to be thickening, which has long puzzled astrophysicists since the accidental discovery in the late 1960s (see Meszaros (2006) for review). Regarding the long-duration GRBs (LGRBs), robust associations of the underlying supernovae with a handful of LGRBs (e.g., Galama et al. (1998); Hjorth et al. (2003); Stanek et al. (2003); Malesani et al. (2004); Modjaz et al. (2006); Pian et al. (2006), and collective references in Woosley & Bloom (2006); Zhang (2011)) and the fact that their host galaxies are typically irregular with intense star formation (Fruchter et al. 2006) suggest that they are likely related to the deaths of massive stars and the "collapsar" model has been widely recognized as the standard scenario for LGRBs (Woosley 1993; Paczynski 1998; MacFadyen & Woosley 1999).

In the scenario, the collapsed iron core of a massive star forms a temporary disk around a few $M_\odot$ black hole (BH) and accretes at a high rate ($\sim 0.1 - 10 M_\odot$/s, e.g., Popham et al. (1999); Di Matteo et al. (2002); Kohri et al. (2005); Chen & Beloborodov (2007); Zalamea & Beloborodov (2011) and references therein), whose gravitational binding energy is the driving source of the central engine. Paczynski (1990) and Meszaros & Rees (1992) pioneeringly proposed that pairs of neutrino and anti-neutrino illuminated from the hyperaccreting disks that annihilate into electron and positron (e.g., $\nu + \bar{\nu} \to e^- + e^+$, hereafter "neutrino pair annihilation") can supply sufficient energy to launch GRB outflows by heating material in the polar funnel regions. In addition, it is suggested that the strong magnetic fields in the cores of order of 10^{15} G play also an active role both for driving the magneto-driven jets and for extracting a significant amount of energy from the central engine (e.g., Blandford & Znajek (1977); Mizuno et al. (2004a,b); McKinney (2006); McKinney & Narayan (2007a,b); Komissarov & Barkov (2007); Komissarov & McKinney (2007); Komissarov & Barkov (2009); Barkov & Komissarov (2008); Nagataki (2009), and references therein).

---

[1]http://www.swift.psu.edu/

Although various possibilities including magnetar models (e.g., Dai & Lu (1998); Thompson et al. (2004); Uzdensky & MacFadyen (2007); Bucciantini et al. (2007)) have been proposed so far, there has been no direct evidence to pin down the mechanism of the central engine. This is mainly because it is difficult to extract the information from conventional astronomy by electromagnetic waves, since high-energy photons are absorbed through interactions in the source and by the photon backgrounds. Alternatively, gravitational waves (GWs) are expected to be a primary observable to decipher the mechanism of the engine, because they imprint a live information hidden deep inside the stellar core and they carry the information directly to us without being affected in propagating to the earth.

Currently long-baseline laser interferometers such as LIGO (Abbott et al. 2005), VIRGO[2], GEO600[3], and TAMA300 (Ando & the TAMA Collaboration 2005) are operational (see, e.g., Hough et al. (2005) for a recent review). For these detectors, core-collapse supernovae (CCSNe) have been proposed as one of the most plausible GW sources, therefore an extensive study of the GW predictions based on sophisticated numerical modeling has been carried out so far (see, for example, Ott (2009); Fryer & New (2011); Kotake (2011) for recent reviews). It is noted however that most of them have paid attention to CCSNe that leave behind neutron stars (NSs) after explosions. For a reliable prediction of GWs from CCSNe, one needs to perform multi-D hydrodynamic simulations equipped with a precise neutrino transport scheme which follows the dynamics starting from stellar core-collapse, core-bounce, through shock-stall and subsequent growth of hydrodynamic instabilities, the neutrino-driven shock revival, to stellar explosion in a consistent manner. This is one of the most challenging subjects in computational astrophysics (e.g., Janka et al. (2007)).

But the numerical modeling to test the collapsar scenario could be much more demanding. One needs to trace a new path that bifurcates from the above story after bounce, namely to the BH formation (phase 1), evolution of the surrounding accretion disk including energy deposition to the polar funnel region by neutrinos and/or magnetic fields (phase 2), to the launching of the fireballs (phase 3)[4]. This apparently necessitates the multidimensional magnetohydrodynamic (MHD) simulations not only with general relativity (GR) for handling the BH formation, but also with the multi-angle neutrino transfer for treating highly anisotropic neutrino radiation from the disks. In the business of CCSN simulations, the most up-to-date simulations[5] can now follow the multi-angle neutrino transport but limited to a Newtonian

---

[2]http://www.ego-gw.it/

[3]http://geo600.aei.mpg.de/

[4]Here for convenience we call each stage as phase 1, 2, etc.

[5]assisted by accelerating computer powers

case (Hubeny & Burrows 2007; Ott et al. 2008; Sumiyoshi & Yamada 2012), or handle GR with a sophisticated neutrino transport (Müller et al. 2010) but not applicable to a rapidly rotating case (due to the assumption of conformal flatness).

Various approximate approaches have been therefore undertaken in the business of the collapsar simulations. In the phase 1, GR simulations (Shibata et al. 2006) updated to implement a neutrino cooling have reported recently (Sekiguchi & Shibata 2011), in which the dynamics after the BH formation to the formation of accretion disk was first consistently followed. The numerical studies of the phase 2 are concerned with the subsequent evolution of accretion disk and the outflow formation in the polar funnel region till the jets become mildly relativistic. The central BH has been traditionally treated by a fixed metric technique in GR simulations (e.g.,Mizuno et al. (2004a); De Villiers et al. (2005); Hawley & Krolik (2006); McKinney & Narayan (2007b); Komissarov & McKinney (2007); Barkov & Komissarov (2008)) or by an absorbing boundary in the Newtonian simulations (e.g., MacFadyen & Woosley (1999); Proga et al. (2003); Fujimoto et al. (2006); Nagataki et al. (2007); López-Cámara et al. (2009, 2010) or special relativistic simulations (e.g., Harikae et al. (2009)). As for the microphysics in these simulations, except for Fujimoto et al. (2006); Nagataki et al. (2007); Harikae et al. (2009); Shibata et al. (2007), a realistic nuclear equation of state (EOS) has been replaced by a very phenomenological one (like a gamma-law or polytrope) and the neutrino cooling (and heating) has been often neglected for simplicity. Numerical studies of the phase 3 are mainly concerned with the dynamics later on, namely, the jet propagation to the breakout from the star, by assuming a manual energy input to the polar funnel region (see, e.g., Aloy et al. (2000); Zhang et al. (2003); Lazzati & Begelman (2009); Nagakura et al. (2011a,b) and references therein). All of the studies mentioned above may be regarded as complimentary in the sense that the different epochs are focused on, with the different initial conditions for the numerical modeling being undertaken.

To the best of our knowledge, Ott et al. (2011) is the only work which extracted the GW signals based on their collapsar simulations (in the phase 1). Based on their three-dimensional (3D) GR simulations of a 75 $M_\odot$ star with the use of a polytropic EOS, they pointed out that the significant GW emission is associated at the moment of the black hole formation, which can be a promising target of the advanced LIGO for a Galactic source. In contrast to such a paucity of the GW predictions based on numerical simulations of collapsars, a number of semi-analytical estimates have been reported so far, which predict a significantly strong GW emission due to possible density-inhomogeneities (Mineshige et al. 2002), bar or fragmentation instabilities in the collapsar's accretion torii (e.g., van Putten (2001); Davies et al. (2002); Fryer et al. (2002); Kobayashi & Mészáros (2003); Piro & Pfahl (2007); Corsi & Mészáros (2009), and collective references in Fryer & New (2011)), and the precession of the disks due to GR effects (Romero et al. 2010; Sun et al. 2012). The predicted

GW amplitudes are typically high enough be visible to advanced-LIGO class detectors for a 100 Mpc distance scale, which is about four orders-of-magnitudes larger than the numerical estimate at the black formation (Ott et al. 2011). In addition to these GWs produced by non-spherical matter motions, Hiramatsu et al. (2005); Suwa & Murase (2009) pointed out that anisotropic neutrino emission from accretion disk could be the source of GWs from collapsars, which was originally proposed as an equally important GW source to the matter GW in the context of CCSNe (Epstein 1978). Since these GWs from collapsars would be a smoking-gun signature of the central engine in coincident with the conventional electromagnetic messengers as well as neutrinos[6], it will be very important to put forward theoretical predictions of GW signals based on the collapsar simulations, as has been done in the business of CCSNe.

In this work, we study possible GW signatures in the hyperaccreting collapsar disks[7] by performing two-dimensional special relativistic (SR) MHD simulations of accretion torii around a black hole. We compute nine models by adding angular momenta and magnetic fields parametrically to a precollapse core of a $35 M_\odot$ progenitor star (Woosley & Heger 2006). As for the microphysics, a realistic equation of state is employed and the neutrino cooling is taken into account via a multiflavor neutrino leakage scheme. In our SR simulations, the central black hole is treated as an absorbing boundary. By doing so, we focus on the GWs generated by asphericities in neutrino emission and matter motions in the vicinity of the accretion disks. To accurately estimate GWs produced by anisotropic neutrino emission, we perform a ray-tracing analysis in GR by a post-processing procedure. By employing a stress formula that includes contributions both from magnetic fields and special relativistic corrections, we study also the effects of magnetic fields on the gravitational waveforms. Then we discuss their detectability by performing a spectrum analysis.

The paper opens up with descriptions of the initial models and numerical methods (section 2). The main results are given in Section 3. We summarize our results and discuss their implications in Section 4.

---

[6]Especially for a nearby GRB source, e.g., Ando et al. (2005).

[7]which corresponds to evolution in the phase 2

2. Numerical Methods and Models
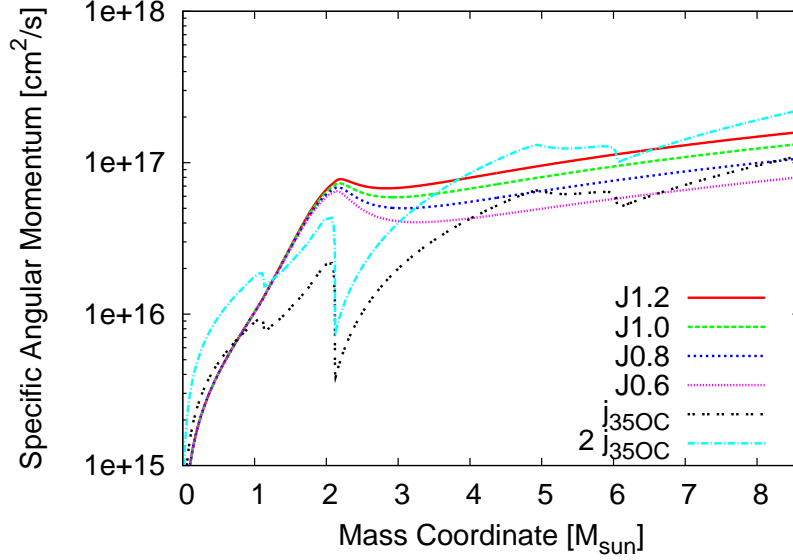
2.1. Initial Models

Fig. 1.— Profiles of the specific angular momentum for model 35OC (Woosley & Heger (2006), labeled by j_{35OC} and the one amplified by a factor of 2 (labeled by $2j_{35OC}$) and for models J0.6, J0.8, J1.0, and, J1.2 (from bottom to top), respectively.

Regarding our precollapse model, we take a $35_\odot$ star (model 35OC) in Woosley & Heger (2006) that is supposed to be one of the most promising GRB progenitor models. To study the effects of rotation systematically, we take the following rotational profiles as

$$\Omega(r,\theta) = \frac{\Omega_0 X_0^4 + \alpha \Omega_{lso}(M(X))X^4}{X_0^4 + X^4},\tag{1}$$

where α, Ω_0, and X_0 are model parameters. $M(X)$ is the mass coordinate at the cylindrical radius ($X = r\sin\theta$), and Ω_{lso} is given by $\Omega_{lso} = j_{lso}/X^2$, where j_{lso} is the specific angular momentum in the last stable orbit of the Schwarzshild BH (e.g., Bardeen et al. (1972); Proga (2005); López-Cámara et al. (2009)). By changing α in the range of $0.6 \leq \alpha \leq 1.2$, we compute 7 non-magnetized models of $\alpha = 0.6, 0.7, 0.8, 0.9, 1.0, 1.1$, and 1.2, by which they are labeled as models J0.6, J0.7, and so on (see Figure 1). To see the effects on magnetic fields, we compute two more models, in which the initial magnetic field ($B_0 = 10^{10}$ G or 10^{11} G) are added to model J0.8 (model J0.8B10 or model J0.8B11), in which the initial field is assumed to be purely poloidal and also assumed to be uniform and parallel to the spin axis.

Figure 1 shows profiles of the initial angular momentum for some models. As shown, our models are taken to possess much more rapid rotation especially in the range of 1 to 4 $M_\odot$ in the mass coordinate compared to the original profile of model 35OC (black dashed line). We set such a rotational profile otherwise the accretion disk cannot survive later than ∼2 s after the onset of gravitational collapse in our simulation. Later on, the accretion disk is swallowed to the central object due to the neutrino cooling which deprives the pressure support in the disk. In this case, one cannot account for the duration of long bursts, the activity of which is typically longer than ~ 2 s, and can last up to tens of minutes. So we experimentally choose to adjust the initial angular momentum as in Equation (1).

Although our models do have higher initial angular momentum, the deviation may not be so serious (compare the light blue line that is for the angular momentum amplified by a factor of 2 in the original progenitor) considering uncertainties in stellar evolution calculations (such as in the treatment of mass-loss, weak interactions, and fluid instabilities (e.g., convection, semiconvection, rotation, and magnetic fields)). To mimic the original progenitor structure, we take X_0 to be the size of the Fe core (≈ 3000 km). By setting $\alpha = 0.8$, $\Omega_0 \approx 1$ rad s^{-1}, the above profile becomes most close to the original profile for the mass coordinates larger than $5M_\odot$. As a side-remark, a most prevailing way is to tune the initial angular momentum to satisfy its local centrifugal force to be several percent-levels of the local gravitational binding energy (e.g., MacFadyen & Woosley (1999)). Our modeling may be more realistic in the sense that the assumed initial angular momentum profiles capture the basic trend obtained in the current progenitor models.

2.1.1. Hydrodynamics

As already mentioned in the introduction, a number of Newtonian and SR collapsar simulations in the phase 2 have conventionally focused on the evolution of the collapsar disks by treating the central BH as an absorbing boundary. Following the tradition of setting the boundary from the beginning of the simulation, we also initially impose an absorbing inner-boundary condition at the radius of $max(10$ km$, 2r_g)$ with r_g is the Schwarzschild radius that is estimated by the accumulating mass inside the inner-boundary. Then we solve the dynamics outside the inner boundary up to the outer boundary of the computational domain (30000 km in radius) by our SRMHD code assuming axisymmetry and equatorial symmetry (see Harikae et al. (2009) for more details). In our 2D simulations, spherical coordinates are employed with logarithmic zoning in the radial direction (r) and regular zoning in the polar direction ($0 \leq \theta \leq \pi/2$). The computational domain is covered by $300(r) \times 40(\theta)$ mesh points. Regarding the microphysics, a realistic nuclear equation of state by Shen et al.

(1998) is included and the neutrino cooling is treated by a multi-flavor leakage scheme (e.g., Epstein & Pethick (1981); Rosswog & Liebendörfer (2003); Kotake et al. (2003a), see Takiwaki et al. (2009) for more details). The gravitational potential is estimated by the sum of the Paczynski & Witta-type potential which mimics the gravitational pull from the central BH and the self-gravity of material outside the excised region that is determined by the Poisson equation (see equations (5) and (6) in Harikae et al. (2009)). In this paper, we examine numerical models without viscosity like the alpha prescription (see, however, MacFadyen & Woosley (1999); Lindner et al. (2010); López-Cámara et al. (2010)).

2.2.   Extraction of Gravitational Waveforms

2.2.1.   GWs from matter motions

To extract the gravitational waveforms from matter motions and magnetic fields, we employ the stress formulae derived in Takiwaki & Kotake (2011); Kotake et al. (2004). For convenience, we shortly summarize them in the following.

In our axisymmetric case, the non-vanishing quadrupole term is only the plus mode (h_+) in the metric perturbation (e.g., Mönchmeyer et al. (1991)), which can be written as,

$$h(\boldsymbol{X}, t) = \frac{1}{8}\sqrt{\frac{15}{\pi}} \sin^2\theta \frac{A_{20}^{E2}\left(t - \frac{R}{c}\right)}{R}, \tag{2}$$

(e.g., Thorne (1980)). The quadrupole amplitude of matter GWs; $A_{20\,\mathrm{matter}}^{\mathrm{E2}}$ that consists of the following three parts,

$$A_{20\,(\mathrm{matter})}^{\mathrm{E2}} = A_{20\,(\mathrm{hyd})}^{\mathrm{E2}} + A_{20\,(\mathrm{grav})}^{\mathrm{E2}} + A_{20\,(\mathrm{mag})}^{\mathrm{E2}}. \tag{3}$$

The first term in Equation (3) represents the contribution from non-spherical hydrodynamic motions, which is expressed by

$$\begin{aligned} A_{20\,(\mathrm{hyd})}^{\mathrm{E2}} &= \frac{G}{c^4}\frac{32\pi^{3/2}}{\sqrt{15}}\int_0^1 d\mu \int_0^\infty r^2\,dr \\ &\times \rho_* W^2(v_r{}^2(3\mu^2 - 1) + v_\theta{}^2(2 - 3\mu^2) - v_\phi{}^2 - 6v_r v_\theta\,\mu\sqrt{1 - \mu^2}), \end{aligned} \tag{4}$$

in which ρ_* is the effective density defined as,

$$\rho_* = \rho + \frac{e + p + |b|^2}{c^2}. \tag{5}$$

Here ρ, e, p, c, and G, denotes the baryon density, internal energy, pressure, the speed of light, and gravitational constant, respectively, and $|b|^2 = b^\mu b_\mu$ is related to the energy density

of the magnetic fields with b_μ representing the magnetic field in the laboratory frame (e.g., Takiwaki et al. (2009)). $W = 1/\sqrt{1 - v^k v_k}$ is the Lorentz boost factor with v_k denoting the spatial velocity in the spherical coordinates ($i = r, \theta, \phi$). $\mu = \cos\theta$ is a directional cosine. The second term in Equation (3) represents the contribution from the gravity as,

$$
\begin{aligned}
A^{\mathrm{E2}}_{20\,(\mathrm{grav})} =\ & \frac{G}{c^4} \frac{32\pi^{3/2}}{\sqrt{15}} \int_0^1 d\mu \int_0^\infty r^2\, dr \\
& \times \left[\rho h (W^2 + (v_k/c)^2) + \frac{2}{c^2} \left(p + \frac{|b|^2}{2} \right) - \frac{1}{c^2} \left((b^0)^2 + (b_k)^2 \right) \right] \\
& \times \left[-r \partial_r \Phi (3\mu^2 - 1) + 3 \partial_\theta \Phi\, \mu \sqrt{1 - \mu^2} \right],
\end{aligned}
\tag{6}
$$

where Φ denotes the gravitational potential of the self-gravity. The last term in Equation (3) is the contribution from the magnetic fields as,

$$
\begin{aligned}
A^{\mathrm{E2}}_{20\,(\mathrm{mag})} =\ & -\frac{G}{c^4} \frac{32\pi^{3/2}}{\sqrt{15}} \int_0^1 d\mu \int_0^\infty r^2\, dr \\
& \times [b_r{}^2 (3\mu^2 - 1) + b_\theta{}^2 (2 - 3\mu^2) - b_\phi{}^2 - 6 b_r b_\theta \mu \sqrt{1 - \mu^2}].
\end{aligned}
\tag{7}
$$

Here, we write the total gravitational amplitude as follows for later convenience,

$$
h^{\mathrm{TT}}_{(\mathrm{matter})} = h^{\mathrm{TT}}_{(\mathrm{hyd})} + h^{\mathrm{TT}}_{(\mathrm{mag})} + h^{TT}_{(\mathrm{grav})},
\tag{8}
$$

where the quantities of the right hand of the equation are defined by combining Equations (2) and (3) with Equations (4), (6), and (7). Note that by dropping $O(v/c)$ terms, the above formulae reduce to the conventional quadrupole formula employed in the Newtonian simulations (e.g., Mönchmeyer et al. (1991)). In the collapsar disk that we pay attention in this work, the condition of $v_\phi \gg v_\theta, v_r$ in Equation (4) is generally satisfied inside the disk. If the disk is perfectly in a stationary state, which means the centrifugal force ($\sim \rho v_\phi^2$) balance with the gravitational forces (e.g., Equation (6)), no GWs can be emitted. As will be explained later, the disk attains mass continuously due to mass-accretion whose specific angular momentum increases outward (e.g., Figure 1). This is the primary reason of generating non-zero matter GWs from axisymmetrically but dynamically rotating collapsar disks. In the following computations, we assume that the observer is located in the equatorial plane ($\theta = \pi/2$ in Equation (2)), and also that the distance to the GW source is comparable to nearly GRB-associated core-collapse supernovae ($R = 100$ Mpc) unless stated otherwise.

2.2.2. GWs from anisotropic neutrino emission

To compute the gravitational waveforms from anisotropic neutrino radiation, we follow the formalism pioneeringly proposed by Epstein (1978); Müler & Janka (1997). In the case

of our 2D axisymmetric case, the only non-vanishing component is the plus mode for the equatorial observer,

$$h_\nu = \frac{4G}{c^4 R} \int_0^t dt' \int_0^\pi d\theta' \, \Phi(\theta') \, \frac{dl_\nu(\theta', t')}{d\Omega'}, \tag{9}$$

where $\Phi(\theta')$ depends on the angle measured from the symmetry axis (θ')

$$\Phi(\theta') = \pi \sin\theta' (-1 + 2|\cos\theta'|). \tag{10}$$

As given in Figure 1 of Kotake et al. (2007), this function has positive values in the north polar cap for $0 \le \theta' \le 60°$ and in the south polar cap for $120° \le \theta' \le 180°$, but becomes negative values between $60° < \theta' < 120°$. To determine the anisotropy in neutrino emission (i.e., $dl_\nu/d\Omega$ in Equation (9)), we perform a ray-tracing analysis, which was first proposed to be applicable in the Newtonian gravity (Kotake et al. 2009b,a, 2011) and later improved to be treatable in SR and GR (Harikae et al. 2010b; Harikae et al. 2010a).

Applying the formalism in Lindquist (1966), the Boltzmann equation for the neutrino occupation probability $f_\nu(\epsilon_\nu, \Omega)$ for a given neutrino energy (ϵ_ν) along a specified direction of Ω can be expressed as,

$$\frac{df_\nu(\epsilon_\nu, \Omega)}{d\lambda} = n[Q_e(1 - f_\nu) - \kappa f_\nu] = n[Q_e - \kappa^* f_\nu], \tag{11}$$

where $n(\boldsymbol{x})$ is the proper number density of the external medium with which neutrinos interact and thus measured in its own local rest frame, ϵ_ν is the neutrino energy measured in the local proper frame, λ denotes an affine parameter along the geodesics, Q_e and κ represents neutrino emissivity and absorptivity, and $(1 - f)$ represents the Pauli blocking term (e.g., Harikae et al. (2010a) for more detailed information to derive the equation). Here we consider only ν_e and $\bar{\nu}_e$ for simplicity, and the energy and momentum transfer via neutrino scattering are neglected, which is not only difficult to be treated by the ray-tracing technique but also a major undertaking in the radiative transport problem in general. In the final expression of Equation (11), κ^* is defined to represent the effective absorptivity. As for the opacity sources of neutrinos, electron capture on proton and nuclei, positron capture on neutron, neutrino scattering with nucleon and nuclei, are included (Fuller et al. 1985; Takahashi et al. 1978; Bruenn et al. 2010). Here κ^* is estimated as $\kappa^* = \Sigma[n_{\text{target}} \cdot \sigma(\epsilon_\nu)]$ with n_{target}, $\sigma(\epsilon_\nu)$ being the target number density of each reaction and the corresponding cross sections, respectively.

According to Zink (2008), the formal solution of Equation (11) can be given as

$$f_\nu(\epsilon, \Omega) = \int_{\lambda_0}^{\lambda_{\text{out}}} n(\lambda'') Q_e(\lambda'', \epsilon_\nu) \exp\left[-\int_{\lambda''}^{\lambda_{\text{out}}} n(\lambda') \kappa^*(\lambda') d\lambda'\right] d\lambda'', \tag{12}$$

which is referred to as the rendering equation of the radiation transport problem. We perform a line integral along the geodesics from every point on the surface of neutrinospheres (λ_0) from which neutrinos can escape freely, up to the outer-most boundary of the computational domain ($\lambda_{\rm out}$). On the neutrinospheres, the neutrino distribution function is assumed to take a Fermi-Dirac type $f^{\rm FD}[= 1/(\epsilon_\nu/k_{\rm B}T + 1)]$ with a vanishing chemical potential[8]. For the neutrino energy bins (ϵ_ν), we use 16 logarithmically spaced energy bins reaching from 3 to 300 MeV.

The path integration in Equation (12) is done explicitly along the geodesics. In doing so, we determine each integration step by restricting the maximum change of neutrino opacity for all the neutrino energy-bins to be less than 10 %. By using an adaptive-mesh-refinement approach also, our ray-trace code was proved to safely pass several test problems (see Harikae et al. (2010a) for more details). For the ray-tracing calculation, $300(r) \times 40(\theta) \times 32(\phi)$ meshes points are cast. The radiation field typically changes more slowly than the hydrodynamics. We perform the ray-tracing calculation every 50 hydrodynamic step to reduce the computational cost. Note that the obtained waveforms did not change significantly when the interval is varied as every 100 or 200 step.

With $f(\epsilon_\nu, \Omega)$ at the outer-most boundary, which is obtained by the above procedure, the emergent neutrino energy fluxes along the specified direction of Ω can be estimated,

$$\frac{dl_\nu(\Omega, \epsilon_\nu)}{d\Omega \, dS} = \int f(\epsilon_\nu, \Omega) \cdot (c\epsilon_\nu) \cdot \frac{\epsilon_\nu^2 d\epsilon_\nu}{(2\pi\hbar c)^3}. \tag{13}$$

By summing up the energy fluxes with the weight of the area in the plane perpendicular to the rays ($:dS$), we can find $dl_\nu/d\Omega$ along the specified direction Ω,

$$\frac{dl_\nu(\Omega)}{d\Omega} = \int \frac{dl_\nu(\Omega)}{d\Omega dS} \, dS \tag{14}$$

Repeating the above procedures, $dl_\nu(\Omega)/d\Omega$ can be estimated for all the directions, by which we can find the amplitudes of the GWs from neutrinos through Equation (9).

3. Results

First we pay attention to the properties of GWs as well as the hydrodynamic features in models without magnetic fields.

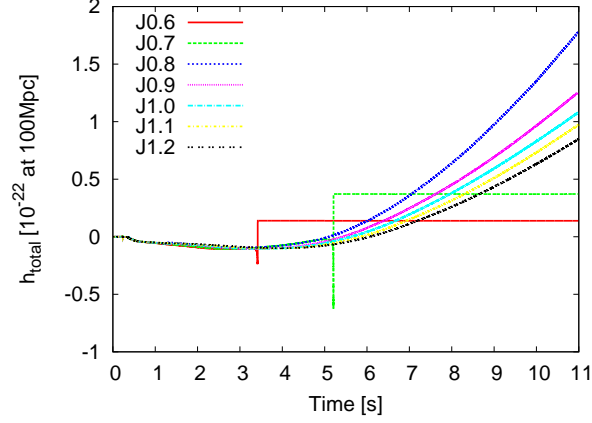[8]$k_{\rm B}$ is the Boltzmann constant

Fig. 2.— Gravitational waveforms from the sum of neutrinos and matter motions for all the non-magnetized models. Note that a collapsar is assumed to be located at the distance of 100 Mpc.

Table 1.   Model Summary

Model	$\Delta t(s)$	$|h_{\max}|(10^{-22})$	$|h_\nu|(10^{-22})$	$E_{\mathrm{GW}}^{\mathrm{total}}(M_\odot c^2)$
J0.6	3.41	0.47	0.14	2.09×10^{-6}
J0.7	5.22	1.15	0.37	5.12×10^{-5}
J0.8	11.0	2.47	1.80	3.91×10^{-3}
J0.9	11.0	3.25	1.22	5.72×10^{-3}
J1.0	11.0	2.86	1.07	4.45×10^{-3}
J1.1	11.0	2.54	0.98	3.56×10^{-3}
J1.2	11.0	2.23	0.86	3.26×10^{-3}
J0.8B10	2.97	0.18	0.037	1.73×10^{-5}
J0.8B11	0.53	0.028	0.0065	9.00×10^{-8}

Note. — Δt represents the simulation time. $|h_{\max}|$ represents the total GW amplitudes at maximum during the simulation time, while h_ν is the neutrino-originated GW at the end of the simulations. $E_{\mathrm{GW},}^{\mathrm{total}}$ is the total radiated energy in the form of the GWs in unit of $M_\odot c^2$. The distance to the source is assumed to be 100 Mpc.
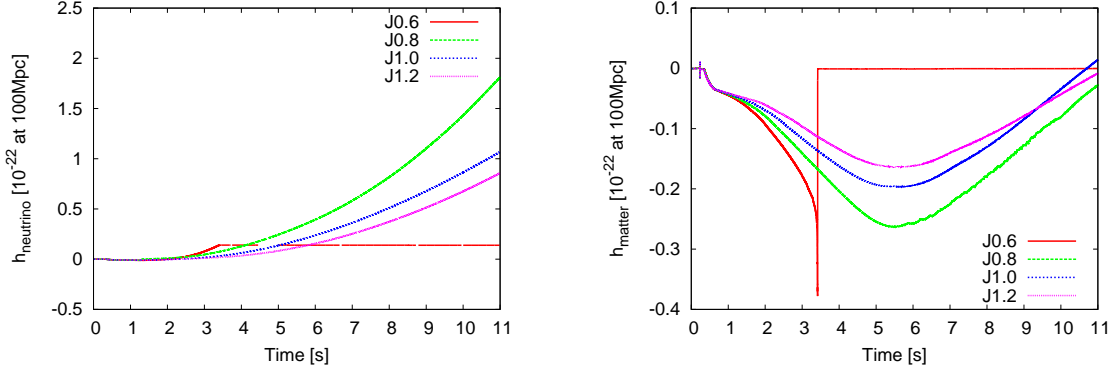
Fig. 3.— Similar to Figure 2 but for the gravitational waveforms only from anisotropic neutrino emission (left panel, e.g., Equation (9)) and only from matter motions (right panel, e.g., Equation (8)). Note that only the selected models are drawn in this figure not to make it messy.

Figure 2 shows the total GW amplitudes for all the computed models without magnetic fields (see also table 1 for a model summary). As seen, the total GW amplitudes generally show a positively growing feature with time. In addition, a sudden disappearance in the signals can be seen for some slowly rotating models (models J0.6 (red line) and J0.7 (green line)). Figure 3 shows the gravitational waveforms contributed only from anisotropic neutrino emission (left panel) and only from matter motions (right panel), respectively. The positively growing trend is shown to come from the neutrino contribution (left), which is much larger than the matter contribution (right). To understand these properties, we first briefly summarize a hydrodynamic evolution of our 2D non-magnetized models in section 3.1. And then in section 3.2, we move on to analyze the reason of the positive growth in the neutrino GWs by performing the ray-tracing analysis. After that, we analyze the matter GWs paying particular attention to the magnetic effects in section 3.3. We then discuss their detectability in section 3.4.

3.1. Hydrodynamic Features

To capture hydrodynamic features in our models, Figure 4 shows the evolution of neutrino luminosities for some selected models. In $t \sim 1.0$ s after we start our simulations ($t \equiv 0$ s), all the models experience rapid infall and the subsequent shock formation in the center,
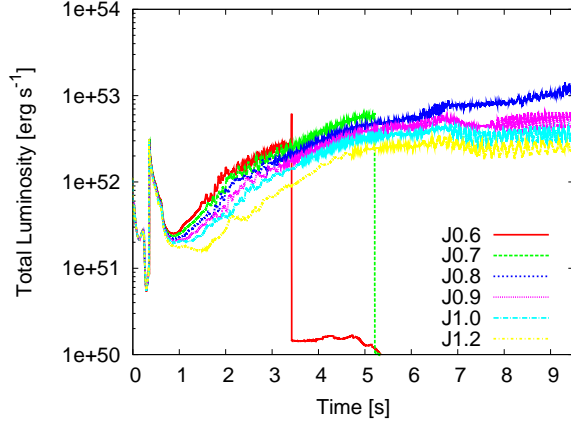
Fig. 4.— Time evolution of neutrino luminosities (the sum of all the neutrino species) for models J0.6, J0.75, J0.8, J0.85, J1.0, and, J1.2, respectively. Note that the time is measured from the epoch when the simulations are started (i.e., the onset of gravitational collapse).

which leads to a drastic increase and the subsequent decrease in the neutrino luminosities[9].

Here we take model J0.8 as a reference, because the precollapse angular momentum is adjusted to be closest to the original progenitor. The top left panel in Figure 5 show a snapshot at $t = 0.42$ s near the shock formation. Note that the accretion mass in this epoch is typically greater than $2 \sim 3 M_\odot$ in the center. The maximum mass of the neutron star of the Shen equation of state is in the same mass range (Shen et al. (1998), see also O'Connor & Ott (2011); Kiuchi & Kotake (2008)). And recent full GR simulations show that the mass of the central object just before collapsing to a BH is typically $\lesssim 2.3 M_\odot$ (e.g., Ott et al. (2011)) with its typical radius of several km (as inferred from their Figure 3). These evidences might support our very crude assumption of the prompt BH formation that is modeled by setting the BH initially in the center, although such assumption can be only tested by full GR simulations using the same progenitor model. Later on, the density configuration (compare the left-half in each panel) deforms to be more oblate with time due to accretion of material with higher angular momentum outside (e.g., Figure 1). As will be explained in the later section, the luminous accretion disk is the primary source of the GWs

---

[9]Note that the shock formation is not because the central density exceeds the nuclear density, but because the matter pressure becomes so high due to compression that it pushes back the ram pressure of accreting material in the vicinity of the inner boundary. In contrast to the state-of-the-art simulations of BH-forming core-collapse supernovae (e.g., Sumiyoshi et al. (2006); Fischer et al. (2009); Ott et al. (2011)), the inability of capturing dynamics correctly especially before the BH formation, is one of major drawbacks in collapsar simulations in general.
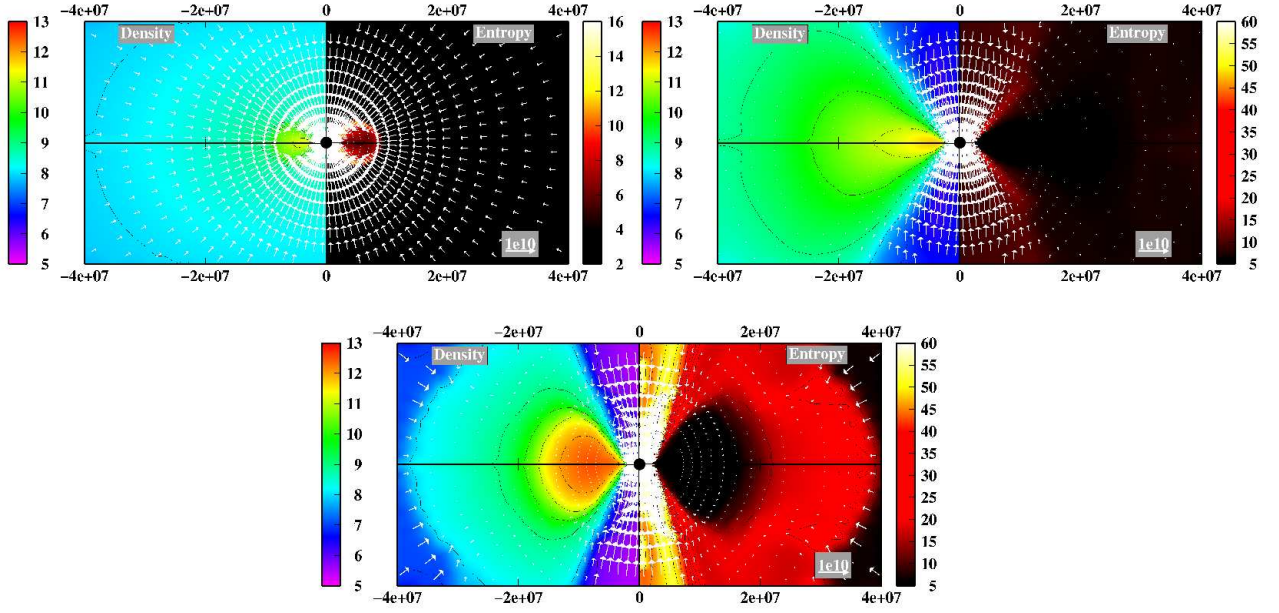
Fig. 5.— Three snapshots characterising the hydrodynamic evolution for model J0.8. The pair panels (top left) are for $t = 0.42$ s, and the top right, bottom panels are for $t = 1.89$ and $t = 9.00$ s, respectively. In the pair panels, the left half in the top panel shows the logarithmic contour of density (in g cm^{-3}), while the right half is for entropy per nucleon in unit of the Boltzmann constant($k_{\rm B}$). The velocity fields are drawn by the white arrows, and the length is normalized by the scale shown in top right edge of the box (i.e. 10^{10}cm s^{-1}). The central black circle represents the inner boundary of our computations.

from anisotropic neutrino emission.

The top right panel in Figure 5 shows a snapshot at $t = 1.89$ s. The bluish regions near along the spin axis of the accretion disk (left-half, density) correspond to the so-called polar funnel regions. The entropy becomes highest near the surface of the accretion disk due to the shock heating when the accreting material hits the wall of the disk (right panel). Comparing Figure 3 (left panel) to Figure 4, the GWs from neutrinos deviate from zero typically later than $t \gtrsim 2 - 3$ s, when the (total) neutrino luminosities become as high as $\sim 10^{52}$erg/s. Later on, the neutrino luminosities show a gradual increase with time, reflecting the increase in the mass accretion to the newly formed accretion disk.
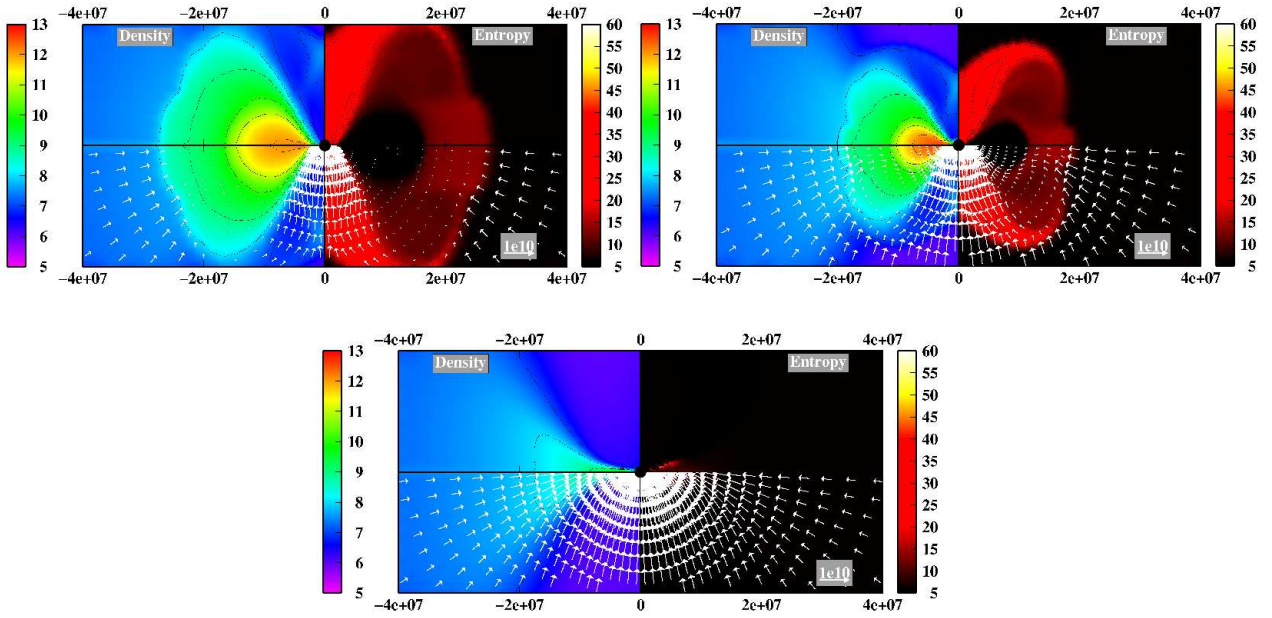
Fig. 6.— Same as Figure 5 but for model J0.6. The top left, top right, and bottom panel is for $t = 3.09$, 3.42, 3.43 s, respectively. For this model, the accretion disk is finally absorbed into the central BH due to its small initial angular momentum (bottom panel), leading to a sudden decrease in the neutrino luminosity (e.g., Figure 4).

In Figure 4, the neutrino luminosity for models J0.6 (red line) and J0.7 (green line) is shown to steeply decrease at ~ 3.3 s and 7.5 s, respectively. This is because the accretion disk is swallowed to the center (bottom panel in Figure 6) mainly because the pressure support in the accretion disk is reduced by the neutrino cooling. The disappearance of the accretion disks is also the reason of the sudden decrease in the GW signals observed both in the neutrino and matter sectors (e.g., Figures 2 and 3). Before the disappearance, the accretion disk is
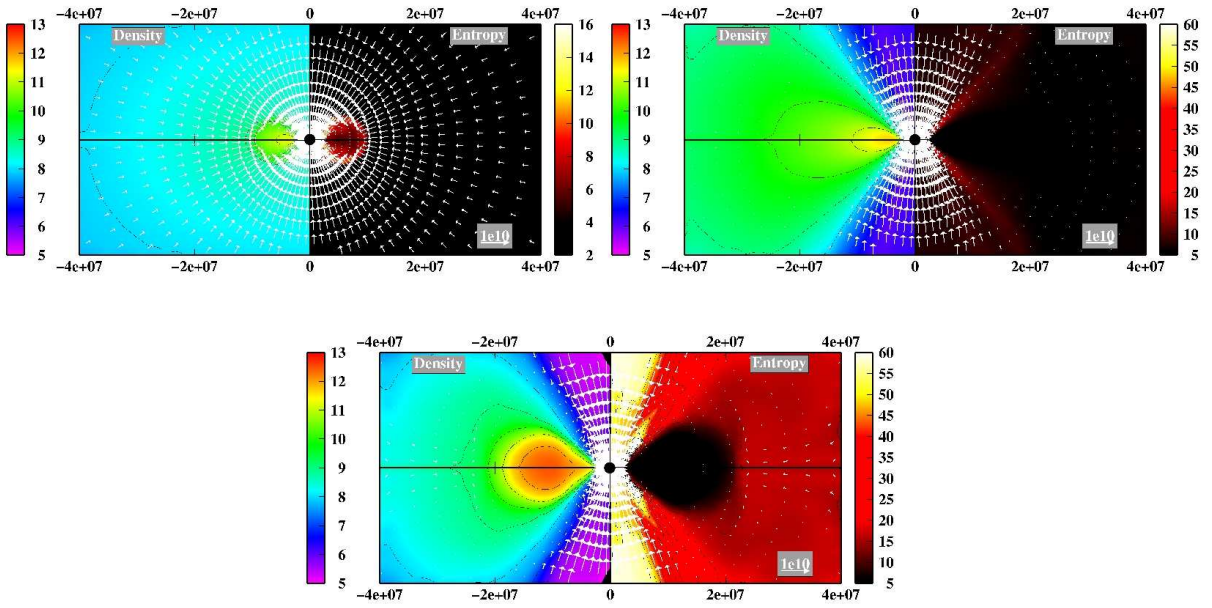
Fig. 7.— Same as Figure 3 but for model J1.1. The top left, top right, and bottom panel is for $t = 0.5,\ 2.4,\ 9.0$ s, respectively. Due to a more larger initial angular momentum than that for Figure 5, the accretion disk is deformed to be more oblate.

observed to show a rapid expansion and contraction (as indicated by the top panels in Figure 6). At the same time, the mass flux on the Lagrange point around the disk changes violently, which may be related to the so-called runaway instability (e.g., Abramowicz et al. (1983); Font & Daigne (2002)). Except for these slowing rotating models, the neutrino luminosities gradually settle to be nearly constant typically later than $t \sim 6\,$s (Figure 4). The saturation of the neutrino luminosity is because the disk is already deleptonized and the neutrino emission there is suppressed (e.g., Harikae et al. (2009) for more details). The neutrino luminosities at this epoch become as high as $10^{52 \sim 53}$ erg s^{-1}, which touches the level of $\sim 10\%$ of the accretion luminosities (see also Chen & Beloborodov (2007); Sekiguchi & Shibata (2011)). Apparently the accretion disk is neutrino-cooling dominated.

From Figure 4, the neutrino luminosity of model J0.8 is shown to be highest (e.g., blue line). Models with higher initial angular momentum have more extended disks due to larger centrifugal forces (compare the bottom panels in Figure 5 and 7), leading to lower density and temperature in the disks. This is the reason that the neutrino luminosities for models J1.0 (light blue line), J1.2 (yellow line in Figure 4) are lower in this order. Reflecting this, the GWs from neutrinos become highest for model J0.8 (left panel of Figure 3, see also $|h_\nu|$ in Table 1). Regarding the matter GWs, it should be noted that their maximum absolute amplitudes are obtained not for the most rapidly rotating model (model J1.2), but for mode J0.8 (right panel of Figure 3). This situation may be akin to the GW signals emitted near core-bounce in core-collapse supernovae (see Kotake et al. (2006, 2011); Ott (2009) for recent reviews). Too much initial angular momentum works to suppress the matter compression leading to the smaller mass-quadrupole moment. As a result, the matter GWs becomes maximum for models with moderately rotating models (e.g., Mönchmeyer et al. (1991); Yamada & Sato (1995); Zwerger & Müller (1997); Kotake et al. (2003b); Shibata & Sekiguchi (2004); Ott et al. (2004, 2007); Dimmelmeier et al. (2002, 2007, 2008); Scheidegger et al. (2010)).

3.2. GWs from Anisotropic Neutrino Emission

In this section, we move on to look more into detail the properties of gravitational waveforms mentioned in the previous section. By taking model J0.8 as a reference, we first focus on the neutrino GWs.

Figure 8 shows the local neutrino energy fluxes ($:dl_\nu/(d\Omega dS)$, Equation (13)) at $t = 9.0$ s (e.g., bottom panel of Figure 5) seen from polar (left) or equatorial direction (right), respectively. Note that the polar direction is taken to be parallel to the spin axis of the accretion disk. The top panel is for the Minkowski geometry, which corresponds to a purely

Newtonian case. Reflecting the shape of the accretion disk in axisymmetry, the contours of the neutrino flux are deformed to be oblate when seen from the equator (top right), while the neutrino flux seen from the polar direction (top left) looks like a superposition of circles in a concentric fashion, the center of which corresponds to the spin axis. Note that the central small cavity in the top left panel corresponds to the inner boundary of our SR simulation.

The middle panels are calculated for the Minkowski geometry including special relativistic corrections (see Harikae et al. (2010a) for more detail). Comparing the middle right to the top right panel, a clear difference is the left-right asymmetry in the middle right panel. This is due to the special relativistic beaming effects. Since the rotational velocity of the accretion disk is perpendicular to the polar direction, the special relativistic beaming effect suppresses the neutrino emission toward the polar region. As a result, the neutrino fluxes are made dark (right-hand side in the middle right panel) because the direction of the rotating material is opposite to the direction to the observer. To study the GR effects on the neutrino luminosity, we place $4M_\odot$ in the central region, which mimics the event horizon of the BH. The effects of the BH spin are examined by setting the Kerr parameter by hand as $a = 0$ and $a = 0.999$ for the Schwarzschild and the extreme Kerr geometry, respectively. The bottom panels of Figure 8 are for the extreme Kerr geometry, which however looks very similar to the middle panels.

For a more detailed comparison, the left panel of Figure 9 shows the neutrino luminosity per solid angle $dL_\nu/d\Omega$ for the Minkowski (indicated by "SR"), Schwarzschild ("GR(a=0))", and extreme Kerr geometry ("GR(a=0.99))", respectively. The most important message in this panel is that in every case, the neutrino luminosity seen from the direction near parallel to the spin axis ($\theta = 0$) becomes higher than the one seen from the equatorial direction ($\theta = \pi/2$). This is because the cross section of the pan-cake like accretion disk seen from the spin axis becomes larger compared to the one seen from the horizontal direction (Figure 8). Remembering again that $\Phi(\theta')$ in Equation (10) is positive near the north and south polar caps, the dominance of the polar neutrino luminosities make the neutrino GWs positive in the polar cap regions (right panel in Figure 9). This is the reason that the neutrino GWs increase monotonically with time (e.g., left panel of Figure 3). Here it is worth mentioning that from neutrino luminosity (L_ν in Figure 4), their typical duration (Δt_ν), anisotropy in the neutrino radiation (α_ν, read from the left panel of Figure 9), the GW amplitudes from neutrinos can be estimated from Equation (9) as

$$h_\nu \approx 10^{-22} \left(\frac{\alpha_\nu}{0.2}\right) \left(\frac{L_\nu}{10^{53} \text{ erg s}^{-1}}\right) \left(\frac{\Delta t_\nu}{10 \text{ s}}\right) \left(\frac{D}{100\text{Mpc}}\right)^{-1}, \tag{15}$$

which is in good agreement with the numerical results (Figure 2).

Comparing to the SR with GR case in the left panel of Figure 9, the neutrino luminosity
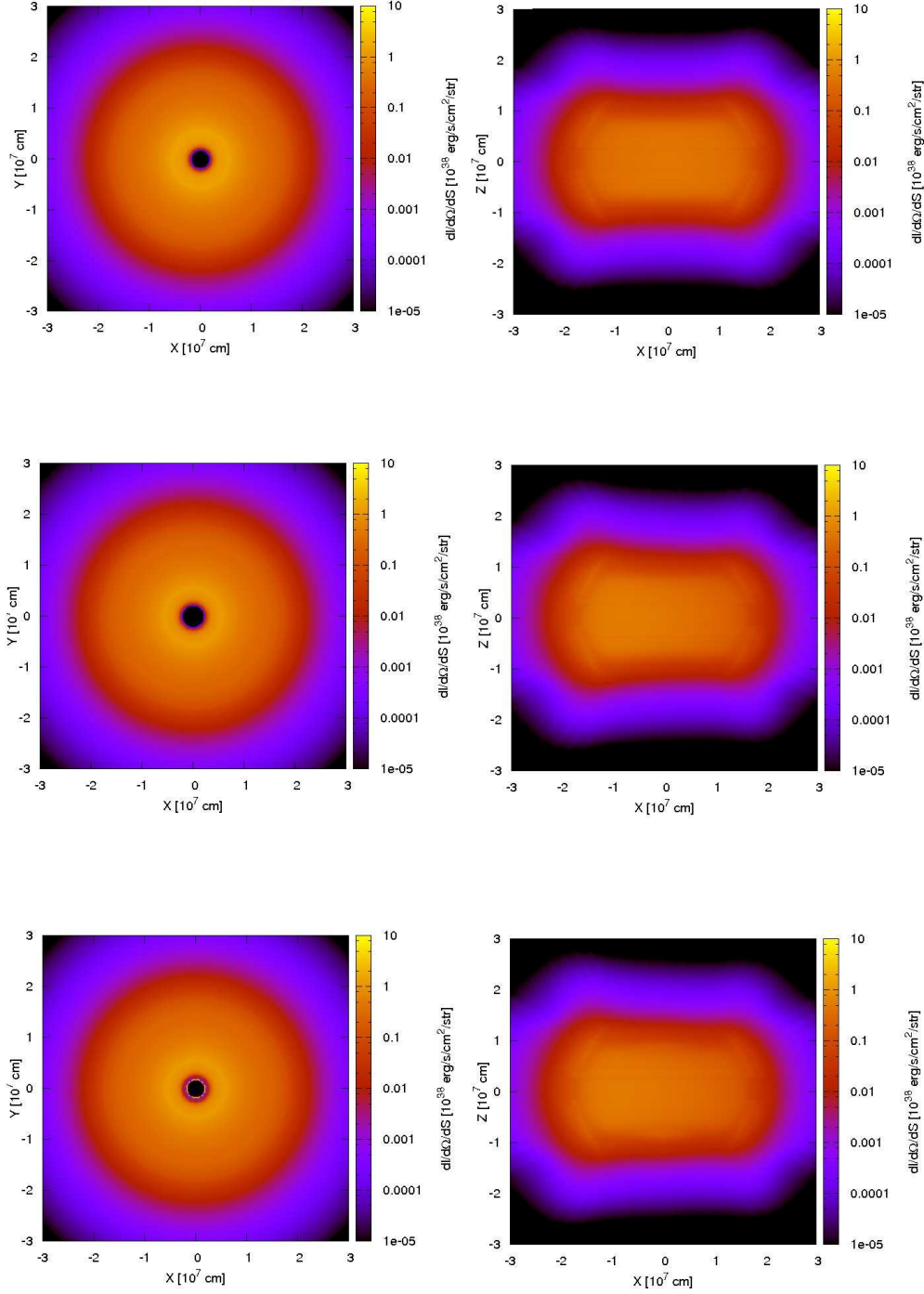
Fig. 8.— The neutrino energy fluxes of $dl_\nu/(d\Omega dS)$ (Equation(13)) seen from polar (left) or equatorial direction (right panels), respectively for model J0.8 at $t = 9.1$ s. The top and middle panels are calculated for the Minkowski geometry without or with special relativistic corrections, and the bottom panels are for the extreme Kerr geometry ($a = 0.999$, see text for more details). Note that the Z axis in the right panels conincides with the spin direction of the accretion disk.
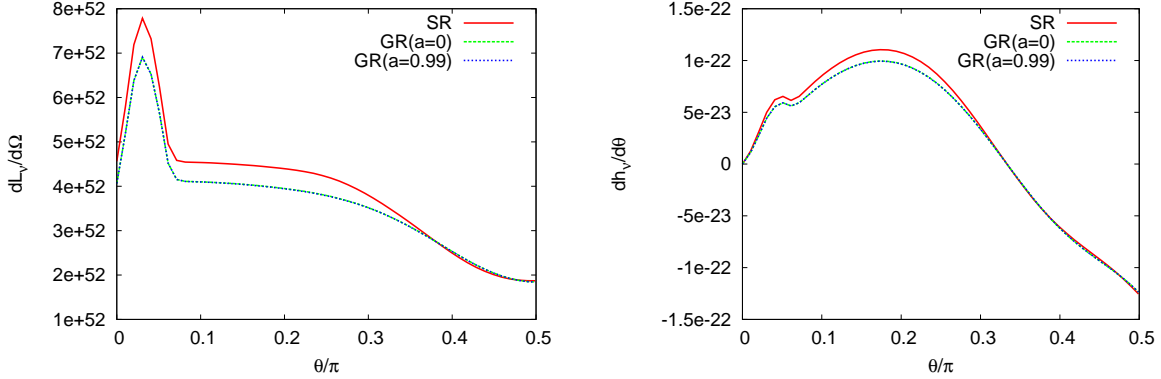
Fig. 9.— The neutrino luminosity per angle (left panel, $dl_\nu/d\Omega$ (Equation (15)) and neutrino GWs per solid angle (right panel) for model J0.8 at t =9.0 s in the case of the Minkowski (indicated by "SR"), Schwarzschild ("GR(a=0))", and extreme Kerr geometry ("GR(a=0.99))", respectively.

becomes smaller by $\sim 20 - 30\%$ in the GR case due to the GR redshift and also due to the bending effects. Comparing the green line with the blue line, the frame-dragging effect due to the BH spin barely affects the emergent neutrino luminosity. This is probably because the GR effect on the neutrino luminosity becomes important only in the central regions very close to the BH (e.g., Figure 15 Harikae et al. (2010a)). Our results indicate that a ray-tracing calculation in the Schwarzschild geometry is at least needed to accurately estimate the neutrino GWs in the collapsar's environment.

3.3. GWs from Matter Motions and Magnetic Fields

Now we shortly analyze the matter GWs in model J0.8. As summarized in section 2.2, the matter GWs are estimated by the sum of the hydrodynamic and gravity parts in Equations (4, 6) for non-magnetized models. Among the kinetic energy terms ($\propto \rho v_i v_j$) in Equation (4), the largest contribution comes from the rotational energy (i.e., $-\rho_* W^2 v_\phi^2$), which is shown in Figure 10 (green line). In contrast to the negative contribution by this term, the gravity part (blue line labeled by "Gravity" in Figure 10) is shown to make a positive contribution. If a star rotates perfectly stationary, the centrifugal forces balance with the gravitational force, leading to no GWs. In the collapsar disk studied in this work, the disk attains mass continuously due to mass-accretion with increasing its specific angular momentum outward. This is the reason why the disk is not perfectly stationary, leading to a non-zero GW emission from matter motions (see pink line labeled by "Matter" in Figure
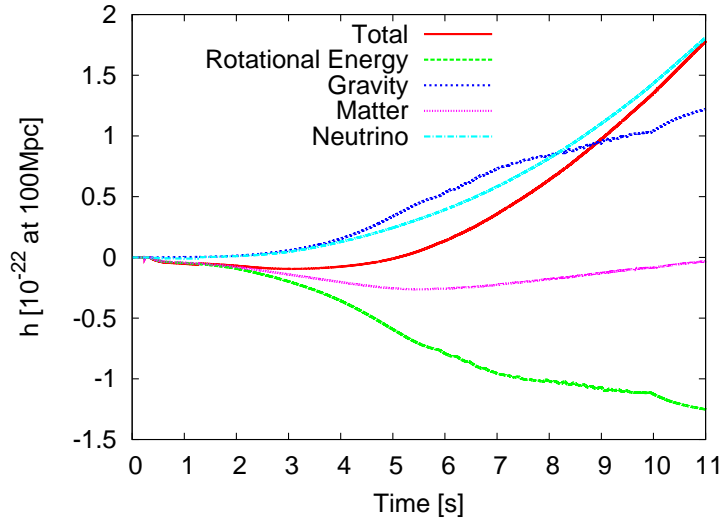
Fig. 10.— The gravitational waveform for model J0.8. "Total" denotes the total amplitudes (the sum of $h_{(\mathrm{matter})}$ in Equation (8) and h_ν in Equation (9)), while "Matter", "Rotational Energy", "Gravity", and "Neutrino" represents the contribution from matter ($h_{(\mathrm{matter})}$ in Equation (8)), rotational energy (see text for the definition), gravity ($h_{(\mathrm{grav})}$ in Equation (8)), and neutrino emission (h_ν in Equation (9)), respectively.

10). However, their GW amplitudes are much smaller compared to those from anisotropic neutrino emission (compare the pink line with the light blue line (neutrino GWs) in Figure 10).

The left panel of Figure 11 shows a normalized contribution of each term in A_{20}^{E2} at $t = 9$ s for model J0.8, which is estimated by the volume integral of A_{20}^{E2} within a given sphere enclosed by certain radius. The region in a radius between 50 km to 160 km is shown to contribute to produce GWs, which corresponds to a high density region in the accretion disk (see the bottom panel in Figure 5). It can be also shown that the radial gradient of the gravitational potential (green line indicated by "Gravity (r)" in the plot) closely cancels with the contribution from the centrifugal force (red line) in the disk. As shown in the right panel of Figure 11, the enclosed mass there becomes as big as $\sim 4M_\odot$ as a result of the hyperaccreting activity lasting ~ 9 s till then, and the typical rotational period there is the order of milliseconds (red line).

Putting these numbers to the standard GW stress formula (e.g., Shapiro & Teukolsky (1983)), an upper bound of the matter GW amplitudes may be estimated as

$$
\begin{aligned}
h_{\text{matter}} & = \frac{2G}{c^4 D}\ddot{I}_{ij} \sim \frac{2G}{c^4 D}\frac{MR^2}{T^2} \\
& \lesssim 10^{-23}\Big(\frac{\epsilon}{0.1}\Big)\Big(\frac{100 \text{ Mpc}}{D}\Big)\Big(\frac{M}{4M_\odot}\Big)\Big(\frac{R}{100 \text{ km}}\Big)^2\Big(\frac{T}{4 \text{ ms}}\Big)^{-2},
\end{aligned} \tag{16}
$$

where D is the distance to the source, $\ddot{I}_{ij}$ is the second time derivative of the quadrupole moment of I_{ij}, M, R, and T represents the typical mass and radius of the accretion disk and the timescale which we may take as the rotational period, respectively, and ϵ is the degree of the nonsphericity, which we take optimistically as 10 % in the case of the accretion disk. This estimate, roughly consistent with the numerical results (e.g., right panel of Figure 3), also shows that anisotropic neutrino emission, producing the GW amplitude on the order of $\approx 10^{-22}$ for a source of 100 Mpc, is the primary source in the long term evolution of collapsars (~ 10 s) (see Equation (15)).

Now we discuss the effects of magnetic fields on the waveforms by taking model J0.8B11 that has a strongest initial magnetic field in our models. In Figure 12, the pink line represents the GWs from magnetic fields (Equation (7)). But, first of all, let us shortly comment on the burst-like feature of the green line (contributed from matter motions) at $t \sim 0.24$ s in the figure. This may look similar to the burst of GWs emitted at the moment of the BH formation possibly followed by a damped sinusoidal oscillation (Seidel (1990, 1991)), but this can be only captured in full GR simulations (Baiotti et al. 2007; Ott et al. 2011; Sekiguchi & Shibata 2011; Kuroda et al. 2012). As already seen in the luminosity plot of Figure 4, the above burst simply corresponds to the shock formation at the center in our SR
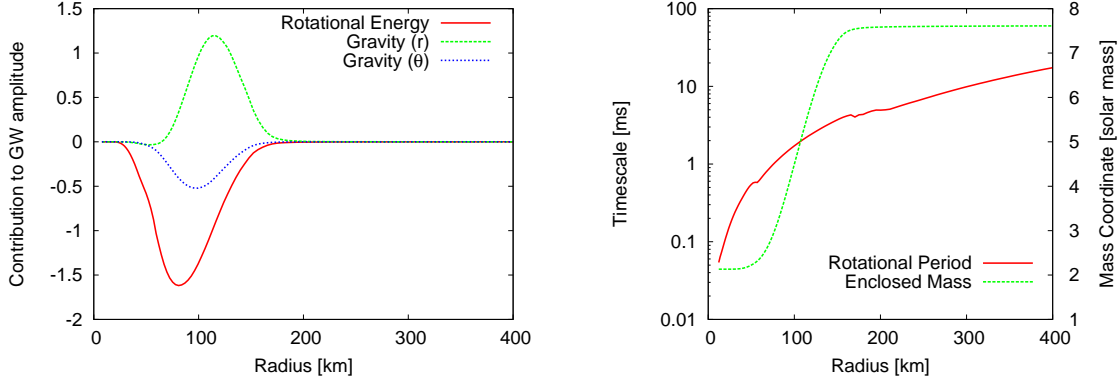
Fig. 11.— Left panel shows a normalized contribution of each term in A_{20}^{E2} (e.g., Equation (3) as similar to Figure 10) as a function of radius for model J0.8 at $t = 9$ s. "Gravity (r/θ)" indicates contributions from radial and lateral derivative of the gravitational potential (corresponding to the last two terms in Equation (6)). Right panel shows the radial profiles of the rotational period (red line) and the enclosed mass normalized by $M_\odot$ (green line), respectively.

models. Back to the main point, we analyze the increasing trend of the GWs from magnetic fields in the following.

The left panel of Figure 13 depicts a snapshot of density (left-half), entropy (right-top) and plasma β (right-bottom, the ratio of magnetic to the matter pressure) at the final simulation time ($t = 541$ ms) for model J0.8B11. The high entropy regions in the slightly off-axis region (seen as reddish in the top right panel) correspond to the magnetohydrodynamically-driven outflows that are pushed outwards by the twisted toroidal magnetic fields (also seen as reddish in the bottom right panel, indicated by "Toroidal").

The right panel of Figure 13 shows contributions to the total GW amplitudes (Equation (9)), in which the left-hand-side panels are for the sum of the hydrodynamic and gravitational part (indicated by "Matter"), namely $\log\left(\pm\left[A_{20\,(\mathrm{hyd})}^{\mathrm{E2}} + A_{20\,(\mathrm{grav})}^{\mathrm{E2}}\right]\right)$ (left top(+)/bottom(−)) (Equations (4,6)), and the right-hand-side panels are for the magnetic part, namely $\log\left[\left(\pm A_{20\,(\mathrm{mag})}^{\mathrm{E2}}\right)\right]$ (right top(+)/bottom(−)) (e.g., Equation (7)). By comparing the top two panels, it can be seen that the positive contribution is overlapped with the regions where the MHD outflows exist. The major positive contribution is from the kinetic term of the MHD outflows with large radial velocities (e.g., $+\rho_* W^2 v_r^2$ in Equation (4)). The magnetic part also contributes to the positive trend (see top right-half in the right panel (labeled by mag(+))). This comes from the toroidal magnetic fields (e.g., $+b_\phi^2$ in Equation (7)), which

dominantly contribute to drive MHD explosions.

Unfortunately, our MHD code becomes numerically unstable when the strong MHD jets propagate to a stellar mantle with decreasing density, which prevents us from studying the resulting GWs in more long run. The neutrino GWs are much smaller than the other GW sources (e.g., Figure 12)) simply due to the shorter simulation time. We expect that the increasing trends by the magnetic fields maintain as the MHD shocks propagate further out (e.g., Takiwaki & Kotake (2011)). To confirm it, we need to implement a numerical technique specially developed to solve the force-free fields, which is major undertaking (e.g., McKinney (2006)).
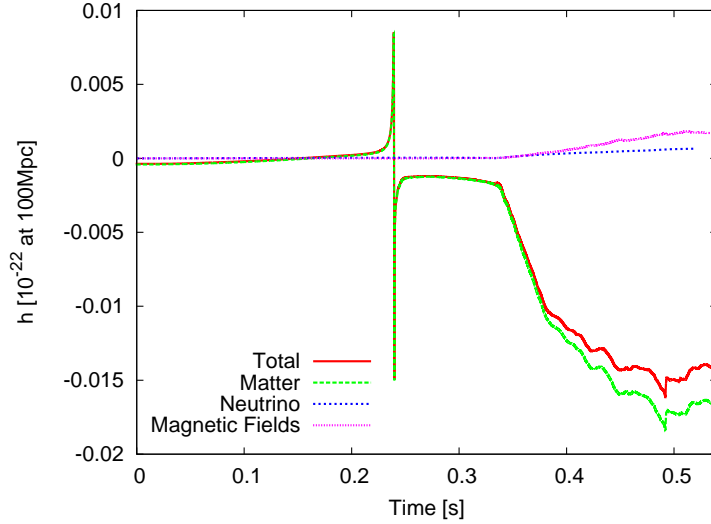

Fig. 12.— Similar to Figure 2 but for model J0.8B11. The pink line represents the GWs from magnetic fields ($h_{(\mathrm{mag})}$ in Equation (8)).

3.4. Detectability

Finally, Figure 14 depicts the GW spectra for models J0.8 (left) and J1.0 (right). The GW spectra in the frequency domain between 1 to 100 Hz becomes slightly larger for model J0.8 than for model J1.0. This reflects a more efficient release of the gravitational binding energy for the moderately rotating case (model J0.8) as already mentioned in sections 3.2 and 3.4. For the cosmological distance scale of GRBs ($\sim$ 100 Mpc), these low frequency GW signals are unfortunately very hard to detect even by the advanced detectors (like the advanced LIGO or KAGRA/LCGT) whose sensitivity is severely limited by the
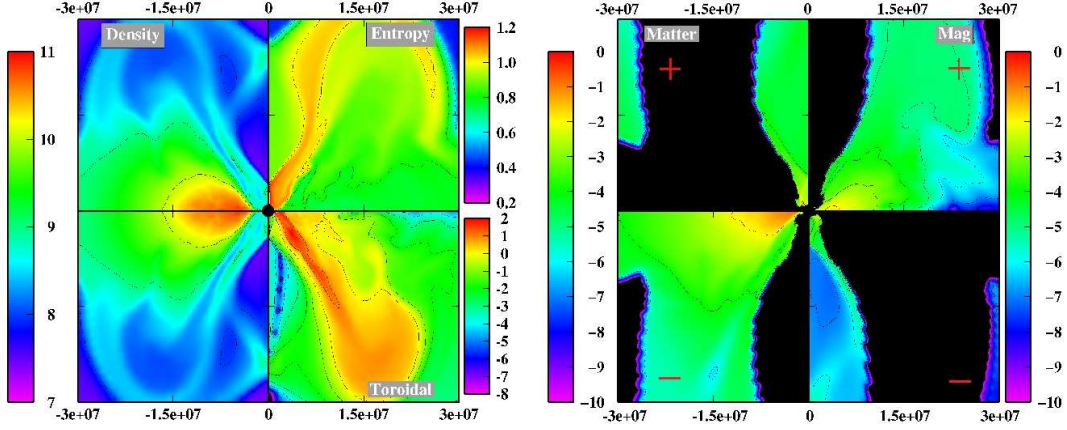
Fig. 13.— Hydrodynamic configuration for model J0.8B11 at $t =$541 ms. In the left panel, the logarithmic density (in g cm^{-3}, left-half), entropy(k_B/baryon, right top), and the ratio of magnetic to the matter pressure (right bottom) are shown. Right panel shows the sum of the hydrodynamic and gravitational parts (indicated by "Matter" in the left-hand side) and the magnetic part (indicated by "Mag" in the right-hand side), respectively. The top and bottom panels represent the positive and negative contribution (indicated by (+) or (-)) to A_{20}^{E2}, respectively (see text for more detail)
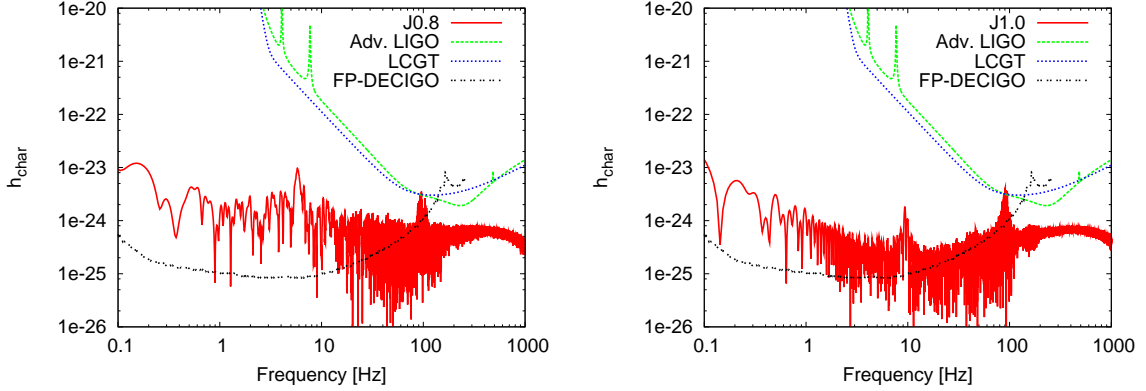

Fig. 14.— Spectral distributions of GWs from matter motions for models J0.8 (left) and J1.0 (right) with the expected detection limits of advanced LIGO (Weinstein 2002), Large-scale Cryogenic Gravitational wave Telescope (LCGT) (Kuroda & LCGT Collaboration 2010), and Fabry-Perot type DECIGO (Kawamura 2006; Kudoh et al. 2006). The distance to the source is assumed to be 100 Mpc. h_{char} is the characteristic gravitational wave strain defined in Flanagan & Hughes (1998). Note that the frequency domain larger than 0.1 Hz is only plotted, since the typical timescale that our simulations covered is 10 s.

seismic noises (Ando & the TAMA Collaboration 2005; Abbott et al. 2005; Weinstein 2002; Kuroda & LCGT Collaboration 2010). A good news is that these signals could be detectable by a recently proposed future space-based interferometer like Fabry-Perot type DECIGO (Kawamura (2006), black line in Figure 14). Two low-luminosity LGRBs were already observed at distances of ~ 40 Mpc (980425, Galama et al. (1998)) and ~ 130 Mpc (060218, Ferrero et al. (2006)). And their local rate, being much higher than that of normal bursts, is expected to be as large $\approx 0.1 D_{100}$ yr^{-1} with D_{100} representing the distance normalized by 100 Mpc (see discussions in Corsi & Mészáros (2009)). Our results suggest that the GW astronomy of collapsars could become reality by the DECIGO-class GW detectors, hopefully near in the future.

4. Summary and Discussion

By performing axisymmetric SRMHD simulations, we investigated possible signatures of GWs in the context of the collapsar model of LGRBs. By cutting out the central BH, we focused on the GWs generated by asphericities in neutrino emission and matter motions in the vicinity of the hyperaccreting disks. Nine models were computed by changing initial angular momenta and magnetic fields parametrically in the precollapse core of a $35M_\odot$ progenitor star. As for the microphysics, a realistic equation of state was employed and the neutrino cooling was taken into account via a multiflavor neutrino leakage scheme. To accurately estimate GWs from neutrinos, we performed a ray-tracing analysis in GR by a post-processing procedure. We studied also the effects of magnetic fields on the gravitational waveforms by employing a stress formula that includes contributions both from magnetic fields and special relativistic corrections. We found that the GW amplitudes from anisotropic neutrino emission shows a monotonic increase with time, whose amplitudes are much larger than those from matter motions of the accreting material. We showed that the increasing trend of the neutrino GWs stems from the excess of neutrino emission in the direction near parallel to the spin axis illuminated from the hyperaccreting disks. We pointed out that a recently proposed future space interferometer like Fabry-Perot type DECIGO would permit the detection of these signals within ≈ 100 Mpc.

Here it should be noted that our 2D simulations cannot capture any non-axisymmetric instabilities so far proposed to provide a strong GW emission in the semi-analytical (e.g., van Putten (2001); Davies et al. (2002); Fryer et al. (2002); Kobayashi & Mészáros (2003); Piro & Pfahl (2007); Corsi & Mészáros (2009)) and in full GR simulations (e.g., Shibata & Sekiguchi (2005); Manca et al. (2007)). Therefore the present results might be regarded to give a lower limit for the possible GW emission in collapsars. To go up the ladders beyond the 2D simulations is very numerical challenging, however, we need to handle it not only to test the outcomes of the proposed ideas about the non-axisymmetric instabilities but also to obtain more accurate waveforms from collapsars.

When studying the formation of BHs and the associated GW signals, the use of a pseudo-newtonian potential can lead to significant errors. This is the reason why we had to limit our discussion only to the asphericities and the resulting GW emission in the vicinity of the accretion disk which is far away from the central object. In studying the dynamics from core-collapse to neutron star, a conformally-flat-condition (CFC) approximation has been often employed to solve the GR equations (Dimmelmeier et al. 2002, 2007, 2008). And it has been tested that such a treatment is very good in capturing the results of full-GR results (e.g., Shibata & Sekiguchi (2003)) for a wide variety of supernova progenitors with neutron star formations. But it may need a further investigation that the approximation is still valid

in applying to collapsars which is a highly aspherical disk-BH system with very dilute polar funnel regions along the rotational axis. Full GR simulations (e.g., Baiotti et al. (2007); Ott et al. (2011); Sekiguchi & Shibata (2011); Kuroda et al. (2012) and references therein) are indeed one of the most important topics pointing to the final frontiers of stellar core-collapse simulations, however, it is generally computationally too expensive at present to follow the late-time collapsar evolution up to ∼10 s, which is a typical duration of long-duration GRBs. Moreover the inclusion of microphysics such as neutrino heating is a major undertaking for the full GR simulations. The Cowling approximation (or the fixed metric approach, e.g., McKinney & Narayan (2007b); Komissarov & McKinney (2007); Barkov & Komissarov (2008)) has been often used in collapsar simulations so far. But it still remains a non-trivial issue how to treat the self-gravity of the accretion disk. Finally, the pseudo-newtonian approach we take in this work cannot unambiguously capture accurate properties of the flows in the vicinity of the BH as well as the associated GW signals. Sacrificing the central regions, such simplified method would be currently only a possible way to follow a long-term evolution (especially for the disk evolution) with including an appropriate treatment of microphysics. Needless to say, these four approaches (full GR, CFC, Cowling, and post-newtonian) may be regarded to be complimentary useful to study the different epochs in the collapsar evolution. For bridging the gaps between them, it may be a good idea to employ the end results of fully GR simulations (e.g., Ott et al. (2011)) in our simulation, which we consider to be the most urgent task to investigate as a sequel of this study.

In a data analysis to extract the true GW signals from the confusing detector noises, it should be of primary importance to take a coincident analysis with the conventional electromagnetic observation as well as neutrinos. What could be the photon and neutrino signatures in our collapsar models ? To answer this question, we need to perform a long-term simulation that bridges continuously the phase 2 and 3 as mentioned in the introduction. For generating neutrino-driven or MHD-driven outflows in numerical simulations of collapsars, the GRMHD simulations including the effects of the neutrino heating are needed, the formulation of which is in a steady progress (e.g., Shibata et al. (2011); Müller et al. (2010); Kuroda et al. (2012)). Assisted by a growing computational power, these advanced simulations would be hopefully practicable by utilizing the next-generation supercomputers. These updates should bring forward not only our understanding the dynamics of the collapsar engines, but also the theoretical predictions of observable multi-messengers (e.g., Ando et al. (2012) for a recent review[10]), including neutrino emission (e.g., Abbasi et al. (2011)) and nucleosynthetic yields (e.g., Fujimoto et al. (2007) and references therein). The neutrino signals emitted from our collapsar models (e.g., from Figure 2 with its typical emergent neutrino energy of ∼ 15 − 20

---

[10]see, Kotake et al. (2012) for a review about multi-messenger perspectives on core-collapse supernovae.

MeV) are visible up to the Local Group ($\sim$ 1 Mpc, Kawagoe et al. in preparation) by future megaton-class detectors (e.g., Hyper-Kamiokande, Memphys, and LBNE), large-scale scintillators (e.g., HALO (Engel et al. 2003), and by liquid-Argon detectors (GLACIER, see Scholberg (2010) for collective references therein). While this work might raise many more questions than it can answer, it definitely makes clear that our understanding of the GWs in collapsars is still in its infancy and that collapsars and the BH-forming supernovae are "gold mine" in which a number of unsettled and fascinating research themes are hidden. We hope that our exploratory results, at least, give momentum to theorists to make the GW prediction based on a more sophisticated numerical modeling of collapsars.

REFERENCES

Abbasi, R., Abdou, Y., Abu-Zayyad, T., et al. 2011, A&A, 535, A109

Alcubierre, M. & Brügmann, B., 2001, Phys. Rev. D, 63, 104006

Abbott et al., M. 2005, Phys. Rev. D, 72, 122004

Abramowicz, M. A., Calvani, M., & Nobili, L. 1983, Nature, 302, 597

Aloy, M. A., Müller, E., Ibáñez, J. M., Martí, J. M., & MacFadyen, A. 2000, ApJ, 531, L119

Ando, M. & the TAMA Collaboration. 2005, Classical and Quantum Gravity, 22, 881

Ando, S., Beacom, J. F., & Yüksel, H. 2005, Physical Review Letters, 95, 171101

Ando, S., Baret, B., Bouhou, B., et al. 2012, arXiv:1203.5192

Baiotti, L., Hawke, I., & Rezzolla, L. 2007, Classical and Quantum Gravity, 24, 187

Bardeen, J. M., Press, W. H., & Teukolsky, S. A. 1972, ApJ, 178, 347

Barkov, M. V. & Komissarov, S. S. 2008, MNRAS, 385, L28

Blandford, R. D. & Znajek, R. L. 1977, MNRAS, 179, 433

Bruenn, S. W., Mezzacappa, A., Hix, W. R., Blondin, J. M., Marronetti, P., Messer, O. E. B., Dirk, C. J., & Yoshida, S. 2010, ArXiv e-prints

Bucciantini, N., Quataert, E., Arons, J., Metzger, B. D., & Thompson, T. A. 2007, MNRAS, L126+

Chen, W.-X. & Beloborodov, A. M. 2007, ApJ, 657, 383

Corsi, A. & Mészáros, P. 2009, ApJ, 702, 1171

Dai, Z. G. & Lu, T. 1998, A&A, 333, L87

Davies, M. B., King, A., Rosswog, S., & Wynn, G. 2002, ApJ, 579, L63

De Villiers, J.-P., Hawley, J. F., Krolik, J. H., & Hirose, S. 2005, ApJ, 620, 878

Di Matteo, T., Perna, R., & Narayan, R. 2002, ApJ, 579, 706

Dimmelmeier, H., Font, J. A., & Müller, E. 2002, Astron. Astrophys., 393, 523

Dimmelmeier, H., Ott, C. D., Janka, H.-T., Marek, A., & Müller, E. 2007, Physical Review Letters, 98, 251101

Dimmelmeier, H., Ott, C. D., Marek, A., & Janka, H. 2008, Phys. Rev. D, 78, 064056

Engel, J., McLaughlin, G. C., & Volpe, C. 2003, Phys. Rev. D, 67, 013005

Epstein, R. 1978, ApJ, 223, 1037

Epstein, R. I. & Pethick, C. J. 1981, Astrophys. J., 243, 1003

Ferrero, P., Kann, D. A., Zeh, A., Klose, S., Pian, E., Palazzi, E., Masetti, N., Hartmann, D. H., Sollerman, J., Deng, J., Filippenko, A. V., Greiner, J., Hughes, M. A., Mazzali, P., Li, W., Rol, E., Smith, R. J., & Tanvir, N. R. 2006, A&A, 457, 857

Fischer, T., Whitehouse, S. C., Mezzacappa, A., Thielemann, F.-K., & Liebendörfer, M. 2009, A&A, 499, 1

Flanagan, É. É. & Hughes, S. A. 1998, Phys. Rev. D, 57, 4566

Font, J. A. & Daigne, F. 2002, MNRAS, 334, 383

Fruchter, A. S., Levan, A. J., Strolger, L., Vreeswijk, P. M., Thorsett, S. E., Bersier, D., Burud, I., Castro Cerón, J. M., Castro-Tirado, A. J., Conselice, C., Dahlen, T., Ferguson, H. C., Fynbo, J. P. U., Garnavich, P. M., Gibbons, R. A., Gorosabel, J., Gull, T. R., Hjorth, J., Holland, S. T., Kouveliotou, C., Levay, Z., Livio, M., Metzger, M. R., Nugent, P. E., Petro, L., Pian, E., Rhoads, J. E., Riess, A. G., Sahu, K. C., Smette, A., Tanvir, N. R., Wijers, R. A. M. J., & Woosley, S. E. 2006, Nature, 441, 463

Fryer, C. L., Holz, D. E., & Hughes, S. A. 2002, ApJ, 565, 430

Fryer, C. L. & New, K. C. B. 2011, Living Reviews in Relativity, 14, 1

Fujimoto, S.-i., Kotake, K., Yamada, S., Hashimoto, M.-a., & Sato, K. 2006, Astrophys. J., 644, 1040

Fujimoto, S.-i., Hashimoto, M.-a., Kotake, K., & Yamada, S. 2007, ApJ, 656, 382

Fuller, G. M., Fowler, W. A., & Newman, M. J. 1985, Astrophys. J., 293, 1

Gal-Yam, A., Fox, D. B., Price, P. A., Ofek, E. O., Davis, M. R., Leonard, D. C., Soderberg, A. M., Schmidt, B. P., Lewis, K. M., Peterson, B. A., Kulkarni, S. R., Berger, E., Cenko, S. B., Sari, R., Sharon, K., Frail, D., Moon, D.-S., Brown, P. J., Cucchiara, A., Harrison, F., Piran, T., Persson, S. E., McCarthy, P. J., Penprase, B. E., Chevalier, R. A., & MacFadyen, A. I. 2006, Nature, 444, 1053

Galama, T. J., Vreeswijk, P. M., van Paradijs, J., Kouveliotou, C., Augusteijn, T., Böhnhardt, H., Brewer, J. P., Doublier, V., Gonzalez, J.-F., Leibundgut, B., Lidman, C., Hainaut, O. R., Patat, F., Heise, J., in't Zand, J., Hurley, K., Groot, P. J., Strom, R. G., Mazzali, P. A., Iwamoto, K., Nomoto, K., Umeda, H., Nakamura, T., Young, T. R., Suzuki, T., Shigeyama, T., Koshut, T., Kippen, M., Robinson, C., de Wildt, P., Wijers, R. A. M. J., Tanvir, N., Greiner, J., Pian, E., Palazzi, E., Frontera, F., Masetti, N., Nicastro, L., Feroci, M., Costa, E., Piro, L., Peterson, B. A., Tinney, C., Boyle, B., Cannon, R., Stathakis, R., Sadler, E., Begam, M. C., & Ianna, P. 1998, Nature, 395, 670

Gehrels, N., Norris, J. P., Barthelmy, S. D., Granot, J., Kaneko, Y., Kouveliotou, C., Markwardt, C. B., Mészáros, P., Nakar, E., Nousek, J. A., O'Brien, P. T., Page, M., Palmer, D. M., Parsons, A. M., Roming, P. W. A., Sakamoto, T., Sarazin, C. L., Schady, P., Stamatikos, M., & Woosley, S. E. 2006, Nature, 444, 1044

Harikae, S., Kotake, K., Takiwaki, T., & Sekiguchi, Y.-i. 2010, ApJ, 720, 614

Harikae, S., Kotake, K., & Takiwaki, T. 2010, ApJ, 713, 304

Harikae, S., Takiwaki, T., & Kotake, K. 2009, Astrophys. J., 704, 354

Hawley, J. F. & Krolik, J. H. 2006, ApJ, 641, 103

Hiramatsu, T., Kotake, K., Kudoh, H., & Taruya, A. 2005, MNRAS, 364, 1063

Hjorth, J. & Bloom, J. S. 2011, ArXiv e-prints

Hjorth, J., Sollerman, J., Møller, P., Fynbo, J. P. U., Woosley, S. E., Kouveliotou, C.,
    Tanvir, N. R., Greiner, J., Andersen, M. I., Castro-Tirado, A. J., Castro Cerón,
    J. M., Fruchter, A. S., Gorosabel, J., Jakobsson, P., Kaper, L., Klose, S., Masetti,
    N., Pedersen, H., Pedersen, K., Pian, E., Palazzi, E., Rhoads, J. E., Rol, E., van den
    Heuvel, E. P. J., Vreeswijk, P. M., Watson, D., & Wijers, R. A. M. J. 2003, Nature,
    423, 847

Hough, J., Rowan, S., & Sathyaprakash, B. S. 2005, Journal of Physics B Atomic Molecular
    Physics, 38, 497

Hubeny, I. & Burrows, A. 2007, ApJ, 659, 1458

Janka, H.-T., Langanke, K., Marek, A., Martínez-Pinedo, G., & Müller, B. 2007, Phys. Rep.,
    442, 38

Kawamura, S. e. a. 2006, Classical and Quantum Gravity, 23, 125

Kiuchi, K. & Kotake, K. 2008, MNRAS, 385, 1327

Kobayashi, S. & Mészáros, P. 2003, ApJ, 589, 861

Kohri, K., Narayan, R., & Piran, T. 2005, ApJ, 629, 341

Komissarov, S. S. & Barkov, M. V. 2007, MNRAS, 382, 1029

—. 2009, MNRAS, 397, 1153

Komissarov, S. S. & McKinney, J. C. 2007, MNRAS, 377, L49

Kotake, K., Iwakami, W., Ohnishi, N., & Yamada, S. 2009a, Astrophys. J., 704, 951

—. 2009b, Astrophys. J. Lett., 697, L133

Kotake, K., Iwakami-Nakano, W., & Ohnishi, N. 2011, ApJ, 736, 124

Kotake, K., Ohnishi, N., & Yamada, S. 2007, Astrophys. J., 655, 406

Kotake, K., Sato, K., & Takahashi, K. 2006, Reports of Progress in Physics, 69, 971

Kotake, K. 2011, arXiv:1110.5107, accepted to Comptes Rendus Physique

Kotake, K., Takiwaki, T., Suwa, Y., et al. 2012, arXiv:1204.2330

Kotake, K., Yamada, S., & Sato, K. 2003a, Astrophys. J., 595, 304

—. 2003b, Phys. Rev. D, 68, 044023

Kotake, K., Yamada, S., Sato, K., Sumiyoshi, K., Ono, H., & Suzuki, H. 2004, Phys. Rev. D, 69, 124004

Kudoh, H., Taruya, A., Hiramatsu, T., & Himemoto, Y. 2006, Phys. Rev. D, 73, 064006

Kuroda, T., Kotake, K., & Takiwaki, T. 2012, arXiv:1202.2487

Kuroda, K. & LCGT Collaboration. 2010, Classical and Quantum Gravity, 27, 084004

Lazzati, D. & Begelman, M. C. 2009, ApJ, 700, L141

Lindner, C. C., Milosavljević, M., Couch, S. M., & Kumar, P. 2010, ApJ, 713, 800

Lindquist, R. W. 1966, Annals of Physics, 37, 487

López-Cámara, D., Lee, W. H., & Ramirez-Ruiz, E. 2009, ApJ, 692, 804

—. 2010, ApJ, 716, 1308

Lü, H.-J., Liang, E.-W., Zhang, B.-B., & Zhang, B. 2010, ApJ, 725, 1965

MacFadyen, A. I. & Woosley, S. E. 1999, Astrophys. J., 524, 262

Malesani, D., Tagliaferri, G., Chincarini, G., Covino, S., Della Valle, M., Fugazza, D., Mazzali, P. A., Zerbi, F. M., D'Avanzo, P., Kalogerakos, S., Simoncelli, A., Antonelli, L. A., Burderi, L., Campana, S., Cucchiara, A., Fiore, F., Ghirlanda, G., Goldoni, P., Götz, D., Mereghetti, S., Mirabel, I. F., Romano, P., Stella, L., Minezaki, T., Yoshii, Y., & Nomoto, K. 2004, ApJ, 609, L5

Manca, G. M., Baiotti, L., DePietri, R., & Rezzolla, L. 2007, Classical and Quantum Gravity, 24, 171

McKinney, J. C. 2006, MNRAS, 367, 1797

McKinney, J. C. & Narayan, R. 2007a, MNRAS, 375, 513

—. 2007b, MNRAS, 375, 531

Meszaros, P. 2006, Reports of Progress in Physics, 69, 2259

Meszaros, P. & Rees, M. J. 1992, MNRAS, 257, 29P

Mineshige, S., Hosokawa, T., Machida, M., & Matsumoto, R. 2002, PASJ, 54, 655

Mizuno, Y., Yamada, S., Koide, S., & Shibata, K. 2004a, Astrophys. J., 606, 395

—. 2004b, Astrophys. J., 615, 389

Modjaz, M., Stanek, K. Z., Garnavich, P. M., Berlind, P., Blondin, S., Brown, W., Calkins, M., Challis, P., Diamond-Stanic, A. M., Hao, H., Hicken, M., Kirshner, R. P., & Prieto, J. L. 2006, ApJ, 645, L21

Mönchmeyer, R., Schaefer, G., Mueller, E., & Kates, R. E. 1991, Astron. Astrophys., 246, 417

Müler, E. & Janka, H.-T. 1997, Astron. Astrophys., 317, 140

Müller, B., Janka, H.-T., & Dimmelmeier, H. 2010, ApJS, 189, 104

Murphy, J. W., Ott, C. D., & Burrows, A. 2009, ArXiv e-prints

Nagakura, H., Ito, H., Kiuchi, K., & Yamada, S. 2011a, ApJ, 731, 80

Nagakura, H., Suwa, Y., & Ioka, K. 2011b, ArXiv e-prints

Nagataki, S. 2009, ApJ, 704, 937

Nagataki, S., Takahashi, R., Mizuta, A., & Takiwaki, T. 2007, Astrophys. J., 659, 512

Nakar, E. 2007, Phys. Rep., 442, 166

O'Connor, E. & Ott, C. D. 2011, ApJ, 730, 70

Ott, C. D. 2009, Classical and Quantum Gravity, 26, 063001

Ott, C. D., Burrows, A., Dessart, L., & Livne, E. 2008, ApJ, 685, 1069

Ott, C. D., Burrows, A., Livne, E., & Walder, R. 2004, Astrophys. J., 600, 834

Ott, C. D., Dimmelmeier, H., Marek, A., Janka, H., Hawke, I., Zink, B., & Schnetter, E. 2007, Physical Review Letters, 98, 261101

Ott, C. D., Reisswig, C., Schnetter, E., O'Connor, E., Sperhake, U., Löffler, F., Diener, P., Abdikamalov, E., Hawke, I., & Burrows, A. 2011, Physical Review Letters, 106, 161103

Paczynski, B. 1990, ApJ, 363, 218

—. 1998, Astrophys. J. Lett., 494, L45+

Pian, E., Mazzali, P. A., Masetti, N., Ferrero, P., Klose, S., Palazzi, E., Ramirez-Ruiz, E., Woosley, S. E., Kouveliotou, C., Deng, J., Filippenko, A. V., Foley, R. J., Fynbo, J. P. U., Kann, D. A., Li, W., Hjorth, J., Nomoto, K., Patat, F., Sauer, D. N., Sollerman, J., Vreeswijk, P. M., Guenther, E. W., Levan, A., O'Brien, P., Tanvir, N. R., Wijers, R. A. M. J., Dumas, C., Hainaut, O., Wong, D. S., Baade, D., Wang, L., Amati, L., Cappellaro, E., Castro-Tirado, A. J., Ellison, S., Frontera, F., Fruchter, A. S., Greiner, J., Kawabata, K., Ledoux, C., Maeda, K., Møller, P., Nicastro, L., Rol, E., & Starling, R. 2006, Nature, 442, 1011

Piro, A. L. & Pfahl, E. 2007, ApJ, 658, 1173

Popham, R., Woosley, S. E., & Fryer, C. 1999, ApJ, 518, 356

Proga, D. 2005, Astrophys. J., 629, 397

Proga, D., MacFadyen, A. I., Armitage, P. J., & Begelman, M. C. 2003, ApJ, 599, L5

Romero, G. E., Reynoso, M. M., & Christiansen, H. R. 2010, A&A, 524, A4+

Rosswog, S. & Liebendörfer, M. 2003, MNRAS, 342, 673

Seidel, E. 1990, Phys. Rev. D, 42, 1884

Seidel, E. 1991, Phys. Rev. D, 44, 950

Scheidegger, S., Käppeli, R., Whitehouse, S. C., Fischer, T., & Liebendörfer, M. 2010, A&A, 514, A51+

Sekiguchi, Y. & Shibata, M. 2011, ApJ, 737, 6

Scholberg, K. 2010, Journal of Physics Conference Series, 203, 012079

Shapiro, S. L. & Teukolsky, S. A. 1983, Black holes, white dwarfs, and neutron stars: The physics of compact objects (Research supported by the National Science Foundation. New York, Wiley-Interscience, 1983, 663 p.)

Shen, H., Toki, H., Oyamatsu, K., & Sumiyoshi, K. 1998, Nuclear Physics A, 637, 435

Shibata, M., Kiuchi, K., Sekiguchi, Y.-i., & Suwa, Y. 2011, ArXiv e-prints

Shibata, M., Liu, Y. T., Shapiro, S. L., & Stephens, B. C. 2006, Phys. Rev. D, 74, 104026

Shibata, M. & Sekiguchi, Y. 2003, Phys. Rev. D, 68, 104020

Shibata, M., Sekiguchi, Y., & Takahashi, R. 2007, Progress of Theoretical Physics, 118, 257

Shibata, M. & Sekiguchi, Y.-I. 2004, Phys. Rev. D, 69, 084024

—. 2005, Phys. Rev. D, 71, 024014

Stanek, K. Z., Matheson, T., Garnavich, P. M., Martini, P., Berlind, P., Caldwell, N., Challis, P., Brown, W. R., Schild, R., Krisciunas, K., Calkins, M. L., Lee, J. C., Hathi, N., Jansen, R. A., Windhorst, R., Echevarria, L., Eisenstein, D. J., Pindor, B., Olszewski, E. W., Harding, P., Holland, S. T., & Bersier, D. 2003, Astrophys. J. Lett., 591, L17

Sumiyoshi, K., & Yamada, S. 2012, ApJS, 199, 17

Sumiyoshi, K., Yamada, S., Suzuki, H., & Chiba, S. 2006, Physical Review Letters, 97, 091101

Sun, M.-Y., Liu, T., Gu, W.-M., & Lu, J.-F. 2012, arXiv:1204.2028

Suwa, Y., & Murase, K. 2009, Phys. Rev. D, 80, 123008

Takahashi, K., El Eid, M. F., & Hillebrandt, W. 1978, Astron. Astrophys., 67, 185

Takiwaki, T., & Kotake, K. 2011, ApJ, 743, 30

Takiwaki, T., Kotake, K., & Sato, K. 2009, Astrophys. J., 691, 1360

Thompson, T. A., Chang, P., & Quataert, E. 2004, Astrophys. J., 611, 380

Thorne, K. S. 1980, Reviews of Modern Physics, 52, 299

Uzdensky, D. A. & MacFadyen, A. I. 2007, Astrophys. J., 669, 546

van Putten, M. H. P. M. 2001, ApJ, 562, L51

Weinstein, A. 2002, Classical and Quantum Gravity, 19, 1575

Woosley, S. E. 1993, ApJ, 405, 273

Woosley, S. E. & Bloom, J. S. 2006, ARA&A, 44, 507

Woosley, S. E. & Heger, A. 2006, Astrophys. J., 637, 914

Yamada, S. & Sato, K. 1995, ApJ, 450, 245

Zalamea, I. & Beloborodov, A. M. 2011, MNRAS, 410, 2302

Zhang, B. 2011, Comptes Rendus Physique, 12, 206

Zhang, W., Woosley, S. E., & MacFadyen, A. I. 2003, ApJ, 586, 356

Zink, B. 2008, Ray-tracing Black Holes, ed. B. Zink

Zwerger, T. & Müller, E. 1997, Astron. Astrophys., 320, 209